

EVIDENCE FOR LARGE SCALE COMPRESSIBLE TURBULENCE IN THE ISM OF CSWA13, A STAR-FORMING LENSED GALAXY AT $Z = 1.87$ WITH OUTFLOWING WIND

ITZHAK GOLDMAN^{1,2}

¹Physics Department, Afeka College, Tel Aviv 6998812, Israel and
²Astrophysics Department, Tel Aviv University, Tel Aviv 6997801, Israel
Version November 8, 2024

Abstract

Recently, [Keerthi Vasana G. et al. \(2024\)](#) presented spatially resolved observations of a wind outflow in CSWA13, a gravitationally lensed Star-Forming galaxy at $z = 1.87$. The gravitational lensing allowed for a substantially improved spatial and kinematic resolution of the wind and of the nebular gas. In this paper we take advantage of the resolved data to test for the existence of turbulence and to study its nature.

We obtained the autocorrelation functions of the two velocity fields, and derived the spatial structure functions of the residual nebular and wind velocities along the major axis of the galaxy. The structure functions, of both velocity fields, reveal the existence of an underlying k^{-2} power spectrum scaling. This scaling suggests the existence of supersonic compressible turbulence. The autocorrelation functions exhibit correlations over scales comparable to the total extent of the velocity fields. Thus, the turbulence is a large scale one. The turbulent timescale corresponding to the largest scale is about 200 Myr, an order of magnitude larger than the estimated age of the wind and of the young stars. This implies that the turbulence in the ISM formed well before the wind and the young stars. Given the large spatial scale of the turbulence, it is plausible that the source of the turbulence is a large scale one e.g. a merger or tidal event that triggered the formation of molecular clouds, in the cores of which, the young stars formed. A steepening of the structure functions on the smaller scales provides an estimate for the effective depth along the line of sight of the turbulent layer. The latter turns out to be $\sim 2kpc$.

Subject headings: galaxy outflows, galaxy evolution, interstellar turbulence

1. INTRODUCTION

High redshift galaxies are characterized by high star formation rates as well as outflowing winds, generated by the young stars or by AGNs, e.g. ([Bournaud et al. 2009](#); [Hoffmann et al. 2022](#); [Rizzo et al. 2021](#); [Sanders et al. 2023](#); [Shah et al. 2022](#)). The high rate of star formation is attributed to the assembly process of the galaxy, e.g. ([Sánchez Almeida et al. 2014](#); [Bennett & Sijacki 2020](#); [Putman 2017](#)). The gas supply can be in the form of inflow from the circum galactic medium (CGM) and also by more violent events such as mergers and tidal interactions.

Observations of high redshift galaxies display velocity dispersions that are usually interpreted as manifestation of turbulence e.g. ([Stark et al. 2008](#); [Burkert et al. 2010](#)). It has been argued that accretion onto disk galaxies can generate large scale turbulence, in particular at the disk outskirts, e.g. ([Forbes et al. 2023](#); [Goldman & Fleck 2023](#)). Turbulence can be generated also by mergers and tidal interactions. To establish the existence of turbulence and moreover, to understand its nature, a power spectrum or structure function of the velocity field are needed. This in turn, demands observations with high enough spatial resolution which, for galaxies at high redshifts, are challenging.

Gravitational lensing can help with this regard. A re-

cent paper ([Keerthi Vasana G. et al. 2024](#)) presented a study of a wind outflow in CSWA13, which is a gravitationally lensed star-forming galaxy at $z = 1.87$. The gravitational lensing allowed for a substantially improved spatial and kinematic resolution. The authors obtained, among other results, two velocity fields along the major axis of the galaxy: the nebular gas velocity traced by the C_{III} emission line, that represents also the velocity of the young stars embedded in the nebular gas, and the wind velocity traced by the Si_{II}^* fluorescent emission line. Each of these velocity fields, exhibits a large scale shear.

In the present paper we set to check whether these velocity fields can be used to test for the existence of turbulence, and if so to obtain its characteristics.

The two residual velocity fields are obtained in section 2. The autocorrelation functions are presented in section 3. In section 4 we obtain the structure functions. Discussion is presented in section 5. In Appendix A, the theoretical structure function of a quantity that is the result of integration along the line of sight direction, is derived. This is used to provide an estimate of the depth of the turbulent layer. In Appendix B, the power spectrum of a quantity that is the result of integration along the line of sight direction, is derived.

2. THE RESIDUAL VELOCITY FIELDS

We digitized the velocity curves of Fig. 8 in Keerthi Vasan G. et al. (2024) and obtained the nebular and wind velocity as functions of position along the galactic major axis. The nebular velocity and the wind velocity exhibit each a large scale shear. We subtracted from each velocity field the corresponding large scale shear, and then removed the remaining mean value. Doing so resulted in two residual velocity fields along the major galactic axis. We derived the autocorrelation function and the structure function for each.

Structure functions rather than power spectra were employed since the former are more detailed on the smaller and medium spatial scales. They are also more reliable at treating data at the borders of the data domain (Nestingen-Palm et al. 2017).

2.1. The residual nebular velocity along the galaxy major axis

We used the Engauge Digitizer Ver.12.1, to mark the nebular velocity of Fig. 8 in Keerthi Vasan G. et al. (2024). The marked observed nebular velocity, offset by 170 km/s, is shown in figure 1.

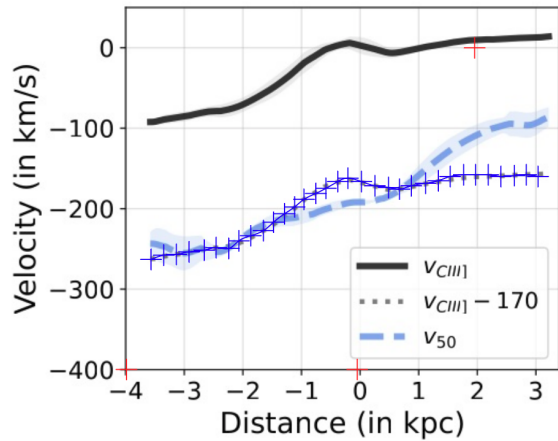


FIG. 1.— The marked nebular velocity, offset by 170 km/s, in units of km/s as function of position along the major axis, in units of kpc .

The Engauge Digitizer yielded the values of the velocity and position at the marked points as seen in figure 2.

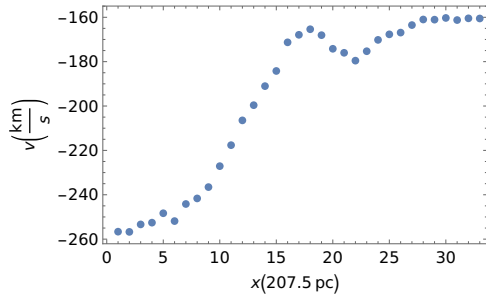


FIG. 2.— The nebular velocity in units of km/s as function of position along the major axis, in units of $207.5pc$.

The nebular velocity possesses a large scale shear of $96.2 km s^{-1}/(6.43kpc)$. After subtracting the shear, and

the remaining mean value, the residual velocity is obtained and is displayed in Fig.3.

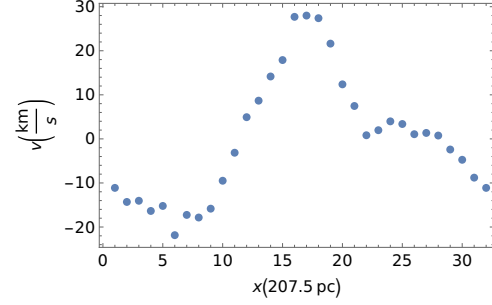


FIG. 3.— The residual nebular velocity in units of km/s as function of position along the major axis, in units of $207.5pc$.

2.2. The residual wind velocity along the galaxy major axis

We follow similar steps in treating the wind velocity. The marked digitized wind velocity of Fig. 8 from Keerthi Vasan G. et al. (2024), is displayed in figure 4.

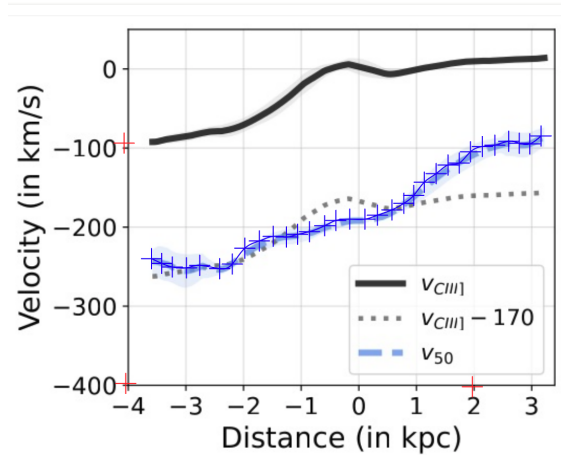


FIG. 4.— The marked wind velocity in units of km/s as function of position along the major axis, in units of kpc .

The Engauge Digitizer yielded the values of the velocity and position of the marked points as seen in Fig. 5.

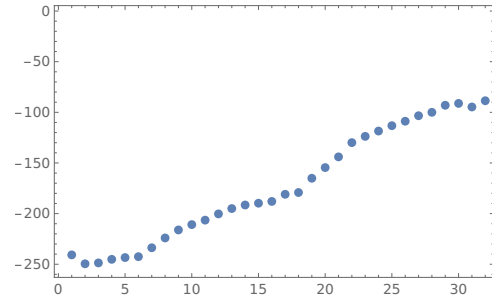


FIG. 5.— The wind velocity in units of km/s as function of position along the major axis, in units of $207.5pc$.

The wind velocity possesses a large scale shear of $152.2 km s^{-1}/(6.43kpc)$. After subtracting the shear, and

the remaining mean value, the residual velocity is obtained and is displayed in Fig.6.

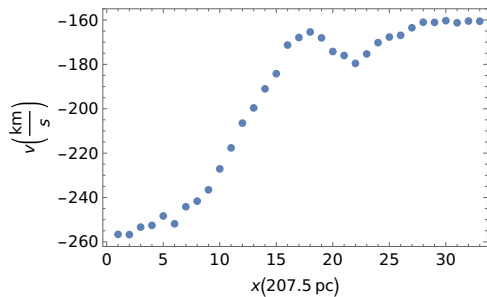


FIG. 6.— The residual wind velocity in units of km/s as function of position along the major axis, in units of $207.5pc$.

3. AUTOCORRELATION FUNCTIONS

The one-dimensional autocorrelation function, $C(x)$, of a residual velocity $v(x)$ (with a zero mean value) is

$$C(x) = \langle v(x+x')v(x') \rangle. \quad (1)$$

The brackets indicate average over all values of x' . Here x denotes the spatial lag between two positions along the galaxy major axis.

3.1. The autocorrelation function of the residual nebular velocity

The computed observational normalized autocorrelation function of the residual nebular velocity is displayed in Fig. 7. It implies that the residual values of the nebular velocity are in fact correlated over large spatial range, comparable to the size of the major axis.

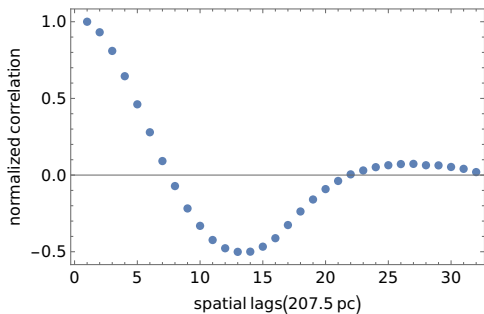


FIG. 7.— The normalized observational autocorrelation function of the residual nebular velocity as function of the spatial lag, in units $207.5pc$.

3.2. The autocorrelation function of the residual wind velocity

Fig.8 presents the normalized autocorrelation function of the wind velocity. It exhibits long range correlation similar to that of the nebular velocity.

Note that while the two residual velocity fields displayed in Fig.3 and in Fig.6 appear to be quite different, their autocorrelation are quite similar, implying underlying spatial correlation that are similar. Long range autocorrelation could be a signature of turbulence. In order to test for the existence of turbulence and understand its nature, we evaluate the structure functions for the two residual velocity fields.

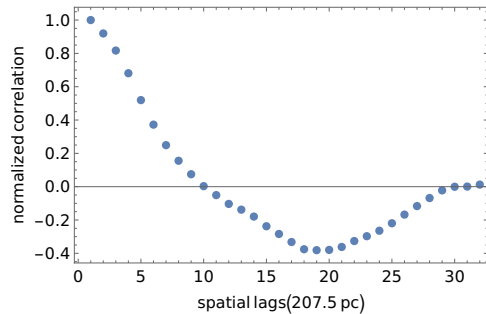


FIG. 8.— The normalized observational autocorrelation function of the residual wind velocity as function of the spatial lag, in units of $207.5pc$.

4. STRUCTURE FUNCTIONS

The one-dimensional structure function of a quantity $f(x)$ defined along a straight line is

$$S_f(x) = \langle (f(x'+x) - f(x'))^2 \rangle = 2C_f(0) - 2C_f(x), \quad (2)$$

with the lag x being the difference between two positions. $C_f(x)$ is the auto correlation function of $f(x)$, with zero mean value, defined as

$$C_f(x) = \langle f(x'+x)f(x) \rangle. \quad (3)$$

In the following, the computed structure functions of the observational residual nebular velocity, and of the residual wind velocity are presented,

4.1. The observational structure function of the residual nebular velocity

Fig.9 displays the structure function of the observational residual nebular velocity. The blue line has a logarithmic slope of 1. The orange line has a logarithmic slope of 2. In Appendix A it is shown that the structure function, evaluated along a lateral line, of a quantity that is an integral over the line of sight direction, increases the logarithmic slope by 1 when the lateral lag is smaller than the effective depth of the turbulent layer. The green line, has a logarithmic slope of $5/3$; that of a Kolmogorov turbulence for the lags smaller than the depth.

The structure function at the largest lag is $2C(0)^2 = 391(km/s)^2$. Thus, the one dimensional rms turbulent velocity is $13.9km/s$. Assuming isotropic turbulence, the three-dimensional turbulent velocity is $24km/s$.

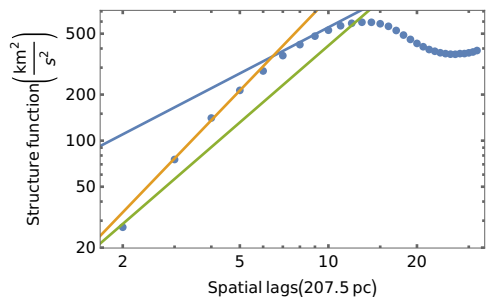


FIG. 9.— The observational structure function of the residual nebular velocity in units of $(km/s)^2$ as function of the spatial lag, in units of $207.5pc$. The asymptotes have logarithmic slopes of 1 and 2. The green line has a logarithmic slope of $5/3$.

4.2. The observational structure functions of the residual wind velocity

Fig. 10 displays the structure function of the residual wind velocity. The blue line has a logarithmic slope of 1. The orange line has a logarithmic slope of 2. This behavior is similar to that of the structure function of the residual nebular velocity. Here too, the green line has a logarithmic slope of $5/3$.

The structure function at the largest lag is $2 < C(0)^2 = 291(km/s)^2$, implying a one-dimensional rms turbulent velocity of $12.1km/s$. Assuming isotropic turbulence, the three-dimensional turbulent velocity is $21km/s$.

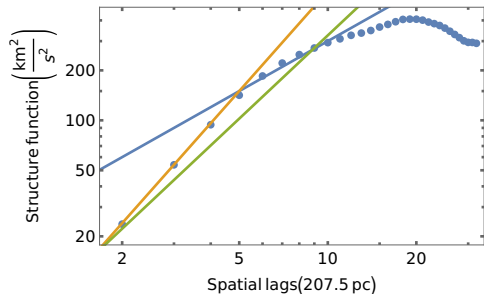


FIG. 10.— The observational structure function of the residual wind velocity, in units of $(km/s)^2$ as function of the spatial lag in units of $207.5pc$. The asymptotes have logarithmic slopes of 1 and 2. The green line has a logarithmic slope of $5/3$.

5. DISCUSSION

5.1. The nature of the turbulence

The observational structure functions of the two residual velocity fields have, each, a logarithmic slope equaling 1 on the large spatial scales and a logarithmic slope of 2 on the small spatial scales. This dependence characterizes compressible turbulence with a one-dimensional power spectrum $\propto k^{-2}$ with k denoting the one-dimensional spatial wave number.

We obtained in appendix A that the logarithmic slope of the structure function equals 1 for spatial lags larger than $0.547D$. In Fig. 9 and Fig. 10 this logarithmic slope holds for spatial lags $2.822 kpc \geq x \geq 1.452 kpc$. The lower limit is $0.547D$, where D is the effective depth of the turbulent region. The upper limit depends on the value of the largest spatial lag. In Appendix A the results were obtained for lags that could extend to infinity. Here, when the lag approaches the largest value, the asymptotic logarithmic slope of 1 is no longer valid.

The compressible power spectrum is steeper than the Kolmogorov power spectrum, which corresponds to subsonic incompressible turbulence with a one-dimensional power law exponent of $-5/3$ and structure function with logarithmic slope of $2/3$ and $5/3$ for the large and small scales, respectively. In Fig. 9 and in Fig. 10, we plotted also the a line with a logarithmic slope of $5/3$ corresponding to Kolmogorov turbulence for the small spatial lags. It is seen that the logarithmic slope of compressible turbulence is favored.

A compressible power spectrum was derived by Burgers (1948) describing a hierarchy of shocks in compressible gas. Compressible turbulence power spectra were observed in HI intensity maps in the Milky Way (MW) galaxy (Green 1993) and in the SMC (Stanimirovic et al.

1999). This power spectrum has been observed also in molecular clouds (Larson 1981; Leung et al. 1982; Dame et al. 1986); in the HII region Sharpless 142 (Roy & Joncas 1985). It has been found in a shocked cloud near the Milky Way galaxy center (Contini & Goldman 2011), and recently in the Gamma ray emission from the large Magellanic Cloud (Besserglik & Goldman 2021). It has been obtained also in numerical simulations e.g. (Passot et al. 1988; Vázquez-Semadeni et al. 1997; Kritsuk et al. 2007; Federrath et al. 2021).

The steeper slope signals that (unlike in the Kolmogorov spectrum) the rate of energy transfer in the turbulence cascade is not constant but decreases with increasing wavenumber. This is expected in a compressible turbulence since part of the energy at a given wavenumber in the cascade, is diverted to compression of the gas. Indeed, a theoretical derivation of the compressible turbulence power spectrum based on this argument has been obtained (Goldman 2021a).

The three-dimensional rms turbulent velocities estimated in section 4. are supersonic, in line with the turbulence being a compressible one.

The turbulence timescale of the largest scale eddies is $\sim L/v_0 \sim 200$ Myr where $L = 6.44 kpc$ is the largest spatial scale and v_0 is the turbulent velocity on this scale. This timescale represents the eddy correlation time on the largest spatial scale and therefore a lower bound on the time span over which the turbulence was created. This time span is an order of magnitude larger than the age of the young stars and the outflowing wind. Thus, the turbulence is older than the young stars and the wind that was created by the latter. The timescales of the large scale shears are about 20 Myr. The emerging picture is that the young stars as well as the wind and the shears were formed on the background of the turbulent interstellar gas.

The autocorrelation functions reveal that the two velocity fields are correlated over a scale of $\sim 6.44 kpc$. The generating source of this large scale turbulence, must itself be correlated over the largest scale of the turbulence, rather than be a collection of smaller scale sources. The probable source is therefore a merger or a close tidal interaction with a smaller galaxy. If the resulting flows are supersonic, the turbulence generated by instabilities in these flows will be supersonic compressible turbulence e.g. (Sparre et al. 2022), as seems to be in the present case.

5.2. The effective depth of the turbulent region

The emitted photons that determine the velocities originate from different depths along the line of sight. The issue of power spectra and structure functions of quantities which are the result of integration along the line-of-sight has been addressed by e.g. (Stutzki et al. 1998; Goldman 2000, 2021b; Lazarian & Pogosyan 2000; Miville-Deschênes et al. 2003a). These authors concluded that when the lateral spatial scale is smaller than the depth of the turbulent layer, the logarithmic slope of the power spectrum steepens by -1 compared to its value when the lateral scale is large compared to the depth. The logarithmic slope of the structure function increases by 1. This behavior was indeed revealed in observational power spectra of Galactic and extra Galactic turbulence (e.g. Elmegreen et al. (2001), Block et al. (2010), Miville-

Deschênes et al. (2003b)) and in solar photospheric turbulence (Abramenko & Yurchyshyn 2020)).

In Appendix A, the theoretical structure function of a quantity that is the result of integration along the line of sight, is obtained. For the specific case of compressible turbulence we found that $D = 1.83x_{tr}$, where D is the effective depth of the turbulent layer and x_{tr} is the observational lag marking the slopes transition in the structure function. The effective depth is the depth of a layer with depth independent of the lateral coordinate, that would yield the observational structure function.

From Fig.9 the observational transition lag for the nebular velocity (1.31 ± 0.04)kpc yielding an effective depth of (2.4 ± 0.07)kpc. The observational transition lag of the wind velocity structure function, from Fig.10 is (1.06 ± 0.04)kpc implying an effective depth of (1.9 ± 0.07)kpc.

The two estimates are close but different. This may occur if the emission lines that determine the velocities emanate from different depths. The values of the effective depth are consistent with the conclusion of Keerthi Vasani et al. (2024) that the wind that, in a spherical shell model, is enclosed in a shell of width ~ 2 kpc. Our results indicate that the nebular gas disk is quite a thick one, this is in line with observations and simulations of high z galaxies, see e.g. (Genzel et al. 2006, 2008).

5.3. Power spectra of the residual velocity fields

To complement the present study we obtain the observational power spectra of the residual velocity fields. The power spectra are the squared absolute value of the discrete Fourier transform of the residual velocity fields. The power spectra of the nebular velocity and the wind velocity are presented in Fig.11 and Fig. 12, respectively. The plots also show straight lines with logarithmic slopes of -2 and -3. For both velocity fields the small wavenumber (large spatial scale) region is not evident.

The power spectra in the figures are functions of the dimensionless wavenumber $q = k_x/k_0$ where $k_0 = \frac{2\pi}{L}$ is the smallest wavenumber corresponding to the largest spatial scale L . In Appendix B, it was obtained that the power spectra are functions of $\mu = \frac{k_x D}{2}$ and that the transition value between the two regimes is at $\mu_{tr} = 1.54$. Thus, the transition wave number is $k_{x,tr} = \mu_{tr} \frac{2}{D}$ implying that the transition dimensionless wavenumber is

$$q_{tr} = \mu_{tr} \frac{2}{D} \frac{L}{2\pi} = 1.54 \frac{L}{\pi D} \quad (4)$$

Employing $L = 6.44$ kpc and the depth values $D = 2.4, 1.9$ kpc for the nebular and wind velocity fields respectively, results in $q_{tr} = 1.31, 1.66$, respectively. This explains why Fig.11 and Fig.12 do not show the small wavenumber region. Thus, the advantage of using structure functions rather than power spectra, in the present case, is clear. If the depth was not that large, then power spectra would be a useful tool.

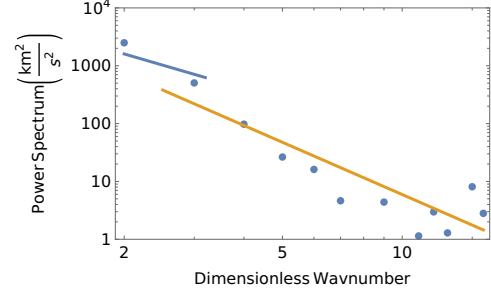


FIG. 11.— The power spectrum of the residual nebular velocity, in units of $(km/s)^2$ as function of the dimensionless wavenumber. The blue line has a logarithmic slope of -2 and the orange line has a logarithmic slope of -3.

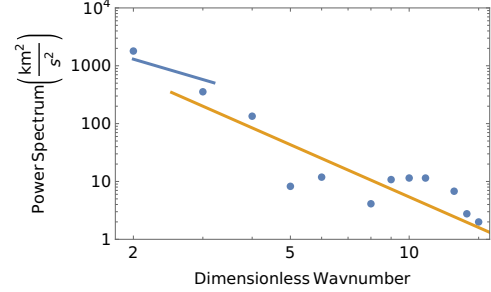


FIG. 12.— The power spectrum of the residual wind velocity, in units of $(km/s)^2$ as function of the dimensionless wavenumber. The blue line has a logarithmic slope of -2 and the orange line has a logarithmic slope of -3.

ACKNOWLEDGMENT

I thank the referee for helpful comments and the Research Authority of Afeka College for support.

APPENDIX

A. THE THEORETICAL STRUCTURE FUNCTION OF A QUANTITY THAT IS THE RESULT OF INTEGRATION ALONG THE LINE OF SIGHT

Consider a function $f(x)$ where x is a straight line in a lateral direction. and is an integral along the line of sight:

$$f(x) = \int_0^D g(x, z) dz. \quad (A1)$$

Here, z is the line of sight coordinate and D the depth. A plane parallel geometry is assumed for simplicity.

The autocorrelation function of $f(x)$ is:

$$\begin{aligned} C_f(x) &= \langle f(x+x')f(x) \rangle = \quad (A2) \\ &= \int_0^D \int_0^D \langle g(x', z)g(x+x', z') \rangle dz dz' = \\ &= \int_0^D \int_0^D C_g(x, z-z') dz dz'. \end{aligned}$$

The autocorrelation function $C_g(x, z-z')$ can be expressed by the two-dimensional power spectrum, $P_2(k_x, k_z)$,

$$C_g(x, z-z') = \int_{-\infty}^{\infty} \int_{-\infty}^{\infty} e^{i(k_x x + k_z (z-z'))} P_2(k_x, k_z) dk_x dk_z. \quad (A3)$$

leading to

$$C_f(x) = \int_{-\infty}^{\infty} \int_{-\infty}^{\infty} e^{ik_x x} P_2(k_x, k_z) \frac{\sin^2(k_z D/2)}{(k_z D/2)^2} dk_x dk_z. \quad (\text{A4})$$

from equations (2) and (A4) follows the expression for the structure function

$$S_f(x, D) \propto \int_0^{\infty} \int_0^{\infty} \sin^2(k_x x/2) \frac{\sin^2(k_z D/2)}{(k_z D/2)^2} P_2(k_x, k_z) dk_x dk_z. \quad (\text{A5})$$

In the case of a turbulence with a one-dimensional power spectrum which is a power law with index $-m$, the two dimensional power spectrum is

$$P_2(k_x, k_z) \propto (k_x^2 + k_z^2)^{-(m+1)/2}. \quad (\text{A6})$$

resulting in

$$S_f(x, D) \propto \int_0^{\infty} \int_0^{\infty} \sin^2(k_x x/2) \frac{\sin^2(k_z D/2)}{(k_z D/2)^2} (k_x^2 + k_z^2)^{-(m+1)/2} dk_x dk_z. \quad (\text{A7})$$

It is convenient to define the dimensionless variables

$$\eta = k_z D/2. \quad ; \quad \mu = k_x D/2. \quad (\text{A8})$$

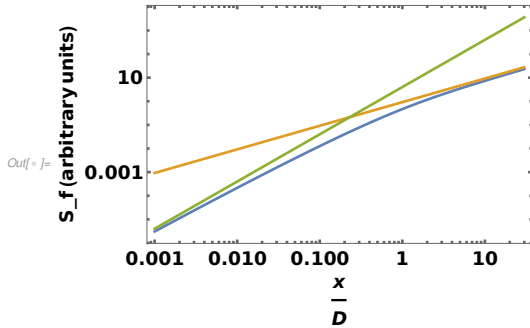


FIG. 13.— Theoretical structure function of a quantity, which is an integral along the line of sight, as function of x/D . The orange line has logarithmic slopes equaling 1 and the green line has a logarithmic slope of 2.

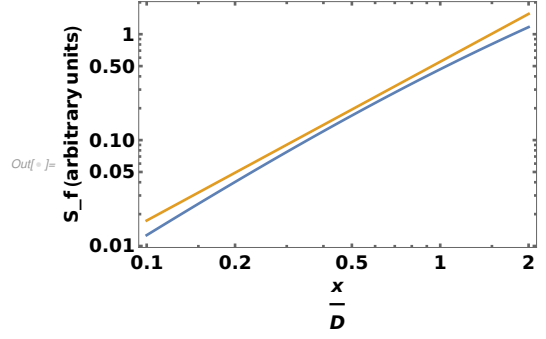


FIG. 14.— Theoretical orange structure function of a quantity, which is an integral along the line of sight, as function of x/D . The straight line has a logarithmic slope of 1.5.

The structure function of equation (A8) can be expressed as

$$S_f(x, D) \propto \int_0^{\infty} I(\mu) \sin^2(\mu x/D) d\mu. \quad (\text{A9})$$

where $I(\mu)$ is

$$I(\mu) = \int_0^{\infty} (\mu^2 + \eta^2)^{-(m+1)/2} \frac{\sin^2 \eta}{\eta^2} d\eta. \quad (\text{A10})$$

Equation (A10) implies that the structure function argument is x/D . Also, inspection of equations (A10) and (A11) reveals that for $x \ll D$ the structure function is proportional to x^m while for $x \gg D$ it is proportional to x^{m-1} .

A numerical solution for the case of $m = 2$ is presented in Fig.13 together with power laws with exponents 1 and 2. In order to find the value of x_{tr}/D , where x_{tr} denotes the transition lag between the two slopes, a power law with exponent of 1.5 is plotted in Fig.14 together with the structure function. The value of x_{tr}/D is taken to be the value for which the logarithmic slope of the structure function equals 1.5, i.e. where the straight line is tangent to the structure function. The result is $x_{tr}/D \sim 0.547$; thus $D \sim 1.83x_{tr}$.

B. THE THEORETICAL POWER SPECTRUM OF A QUANTITY THAT IS THE RESULT OF INTEGRATION ALONG THE LINE OF SIGHT

The 1D power spectrum $P_f(k_x)$ is by definition

$$P_f(k_x) = \int_{-\infty}^{\infty} e^{-ik_x x} C_f(x) dx \quad (\text{B1})$$

From equations (A4) and (A6) follows

$$P_f(k_x) \propto \int_{-\infty}^{\infty} (k_x^2 + k_z^2)^{-(m+1)/2} \frac{\sin^2(k_z D/2)}{(k_z D/2)^2} dk_z \quad (\text{B2})$$

Using Equations (A9) and A(11) we obtain

$$P_f(k_x) = P_f(\mu) = I(\mu) \quad (\text{B3})$$

Thus, the power spectrum is a function of μ . Inspection of equations (A11) and (B3) reveals that for $\mu \ll 1$, $P_f(k_x) \propto k_x^{-m}$, while for $\mu \gg 1$, $P_f(k_x) \propto k_x^{-m-1}$. For the present case of $m = 2$ the power spectrum is plotted in Fig.15. Plotted also are the asymptotes with logarithmic slopes of -2 and -3.

In order to find the transition value μ_{tr} a line with a logarithmic slope of -2.5 is plotted and the value of μ_{tr} is taken to be the tangent point to the power spectrum. From Fig.16 we find that $\mu_{tr} = 1.54$.

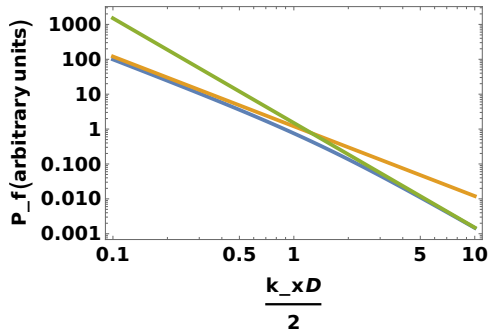


FIG. 15.— Theoretical power spectrum, of a quantity which is an integral along the line of sight, as function of $k_x D/2$. The orange line has a logarithmic slopes equaling -2 and the green line has logarithmic slope of -3.

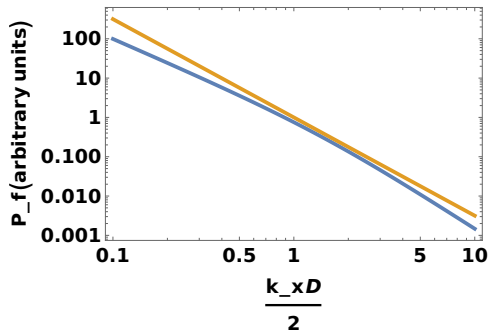


FIG. 16.— Theoretical power spectrum, of a quantity which is an integral along the line of sight, as function of $k_x D/2$. The straight line has a logarithmic slope equaling -2.5.

REFERENCES

- Abramenko, V. I. & Yurchyshyn, V. B. 2020, MNRAS, 497, 5405. doi:10.1093/mnras/staa2427.
- Bennett, J. S. & Sijacki, D. 2020, MNRAS, 499, 597. doi:10.1093/mnras/staa2835
- Besserglik, D. & Goldman, I. 2021, ApJ, 915, 117. doi:10.3847/1538-4357/ac0247.
- Block, D. L., Puerari, I., Elmegreen, B. G., et al. 2010, ApJ, 718, L1. doi:10.1088/2041-8205/718/1/L1.
- Bournaud, F., Elmegreen, B. G., & Martig, M. 2009, ApJ, 707, L1. doi:10.1088/0004-637X/707/1/L1.
- Burgers, j. M. 1948, Advances in Applied Mechanics, 1, 171.
- Burkert, A., Genzel, R., Bouché, N., et al. 2010, ApJ, 725, 2324. doi:10.1088/0004-637X/725/2/2324
- Contini, M. & Goldman, I. 2011, MNRAS, 411, 792. doi:10.1111/j.1365-2966.2010.17719.x.
- Dame, T. M., Elmegreen, B. G., Cohen, R. S., et al. 1986, ApJ, 305, 892. doi:10.1086/164304.
- Elmegreen, B. G., Kim, S., & Staveley-Smith, L. 2001, ApJ, 548, 749.
- Federrath, C., Klessen, R. S., Iapichino, L., et al. 2021, Nature Astronomy, 5, 365. doi:10.1038/s41550-020-01282-z.
- Forbes, J. C., Emami, R., Somerville, R. S., et al. 2023, ApJ, 948, 107. doi:10.3847/1538-4357/acb53e.
- Genzel, R., Tacconi, L. J., Eisenhauer, F., et al. 2006, Nature, 442, 786. doi:10.1038/nature05052
- Genzel, R., Burkert, A., Bouché, N., et al. 2008, ApJ, 687, 59. doi:10.1086/591840
- Goldman, I. & Fleck, R. 2023, MNRAS, 521, 2949. doi:10.1093/mnras/stad1277.
- Goldman, I. 2021a, Physics of Fluids, 33, 071706. doi:10.1063/5.0058074.
- Goldman, I. 2021b, MNRAS, 504, 4493. doi:10.1093/mnras/stab1227.
- Goldman, I. 2000, ApJ, 541, 701.
- Green, D. A. 1993, MNRAS, 262, 327. doi:10.1093/mnras/262.2.327.
- Hoffmann, K., Laigle, C., Chisari, N. E., et al. 2022, MNRAS, 515, 3603. doi:10.1093/mnras/stac1988.
- Kolmogorov, A. 1941, Akademiia Nauk SSSR Doklady, 30, 301.
- Larson, R. B. 1981, MNRAS, 194, 809. doi:10.1093/mnras/194.4.809.
- Keerthi Vasan G., C., Jones, T., Shajib, A. J., et al. 2024, arXiv:2402.00942. doi:10.48550/arXiv.2402.00942.
- Kritsuk, A. G., Norman, M. L., Padoan, P., et al. 2007, ApJ, 665, 416. doi:10.1086/519443.
- Lazarian, A. & Pogosyan, D. 2000, ApJ, 537, 7.
- Leung, C. M., Kutner, M. L., & Mead, K. N. 1982, ApJ, 262, 583. doi:10.1086/160450.
- Miville-Deschênes, M.-A., Levrier, F., & Falgarone, E. 2003a, ApJ, 593, 831.
- Miville-Deschênes, M.-A., Joncas, G., Falgarone, E., et al. 2003b, A&A, 411, 109.
- Shah, E. A., Kartaltepe, J. S., Magagnoli, C. T., et al. 2022, ApJ, 940, 4. doi:10.3847/1538-4357/ac96eb.
- Nestingén-Palm, D., Stanimirović, S., González-Casanova, D. F., et al. 2017, ApJ, 845, 53. doi:10.3847/1538-4357/aa7e78.
- Passot, T., Pouquet, A., & Woodward, P. 1988, A&A, 197, 228.
- Putman, M. E. 2017, Gas Accretion onto Galaxies, 430, 1. doi:10.1007/978-3-319-52512-9_1
- Roy, J.-R. & Joncas, G. 1985, ApJ, 288, 142. doi:10.1086/162772.
- Rizzo, F., Vegetti, S., Fraternali, F., et al. 2021, MNRAS, 507, 3952. doi:10.1093/mnras/stab2295.
- Sánchez Almeida, J., Elmegreen, B. G., Muñoz-Tuñón, C., et al. 2014, A&A Rev., 22, 71. doi:10.1007/s00159-014-0071-1
- Sanders, R. L., Shapley, A. E., Jones, T., et al. 2023, ApJ, 942, 24. doi:10.3847/1538-4357/aca46.
- Shah, E. A., Kartaltepe, J. S., Magagnoli, C. T., et al. 2022, ApJ, 940, 4. doi:10.3847/1538-4357/ac96eb.
- Sparre, M., Whittingham, J., Damle, M., et al. 2022, MNRAS, 509, 2720. doi:10.1093/mnras/stab3171
- Stanimirovic, S., Staveley-Smith, L., Dickey, J. M., et al. 1999, MNRAS, 302, 417. doi:10.1046/j.1365-8711.1999.02013.

Stark, D. P., Swinbank, A. M., Ellis, R. S., et al. 2008, *Nature*, 455, 775. doi:10.1038/nature07294

Stutzki, J., Bensch, F., Heithausen, A., et al. 1998, *A&A*, 336, 697.

Vázquez-Semadeni, E., Ballesteros-Paredes, J., & Rodríguez, L. F. 1997, *ApJ*, 474, 292. doi:10.1086/303432.

This paper was built using the Open Journal of Astrophysics L^AT_EX template. The OJA is a journal which

provides fast and easy peer review for new papers in the **astro-ph** section of the arXiv, making the reviewing process simpler for authors and referees alike. Learn more at <http://astro.theoj.org>.